



Deposited via The University of Sheffield.

White Rose Research Online URL for this paper:

<https://eprints.whiterose.ac.uk/id/eprint/116107/>

Version: Accepted Version

Article:

Nasir, D.S.N.M., Hughes, B.R. and Calautit, J.K. (2017) Influence of urban form on the performance of road pavement solar collector system: symmetrical and asymmetrical heights. *Energy Conversion and Management*, 149. pp. 904-917. ISSN: 0196-8904

<https://doi.org/10.1016/j.enconman.2017.03.081>

Article available under the terms of the CC-BY-NC-ND licence
(<https://creativecommons.org/licenses/by-nc-nd/4.0/>)

Reuse

This article is distributed under the terms of the Creative Commons Attribution-NonCommercial-NoDerivs (CC BY-NC-ND) licence. This licence only allows you to download this work and share it with others as long as you credit the authors, but you can't change the article in any way or use it commercially. More information and the full terms of the licence here: <https://creativecommons.org/licenses/>

Takedown

If you consider content in White Rose Research Online to be in breach of UK law, please notify us by emailing eprints@whiterose.ac.uk including the URL of the record and the reason for the withdrawal request.

1 **Influence of urban form on the performance of road pavement**
2 **solar collector system: symmetrical and asymmetrical heights**

3 **Diana SNM Nasir, Ben Richard Hughes, John Kaiser Calautit**

4 *The University of Sheffield, United Kingdom*

5
6
7 **Abstract**

8 Recent works have highlighted the importance of mitigating the urban heat island effect using
9 innovative technologies. Several studies have emphasised the capabilities of the road pavement solar
10 collector system to dissipate high temperature from the pavement/road surfaces not only to expand its
11 lifecycle but also to reduce the Urban Heat Island effect. This study builds on previous research
12 combining an urban configuration and a road pavement solar collector system in Computational Fluid
13 Dynamics in order to understand the complicated connection of the urban environment and the road
14 pavement. This study investigates the impact of the urban form on the performance of the road
15 pavement solar collector focusing on comparing symmetrical and asymmetrical height of the urban
16 street canyon. A tridimensional de-coupled simulation approach was used to simulate a macro domain
17 (urban environment) and micro domain, which consists of road pavement solar collector pipes.
18 ANSYS Fluent 15.0 was employed with the solar load model, Discrete Ordinate radiation model and
19 Reynold Averaged Navier Stokes with standard k -epsilon equation. The simulation was carried out
20 based on the summer month of June in Milan urban centre, Italy. Results showed a significant
21 variation in the temperature results of road surface in comparing the three configurations. It was also
22 found that there was a significant reduction in the road pavement solar collector system performance
23 when taller building row was behind the first approaching building row. The method presented in this
24 research could be useful for studying the system integration in various urban forms.

25
26
27 **Keyword:** Urban Heat Island, urban street canyon, building simulation, Computational Fluid
28 Dynamics, road solar collector, heat transfer

29
30
31 **Number of words: 8244**

36 **1.0 Introduction and problem statement**

37 Previous related works have emphasised on the significant reduction of wind velocity penetrating the
38 urban street canyon, in particular, canyons oriented perpendicularly to the wind direction [1], causing
39 the rise in the air temperature in between the two narrowed street walls. This urban geometrical
40 configuration was highlighted for its contribution in the formation of the Urban Heat Island (UHI)
41 effect particularly within tight urban planning (tall buildings alongside narrow streets) with less open
42 spaces [2]. Generally; as reported in the review paper of [3], studies of UHI effect have included three
43 observation methods: (i) field measurements, (ii) thermal remote sensing, and (iii) small-scale
44 modelling. Another common approach is ‘simulation’, which includes energy balance and numerical
45 modelling. The study of [4] highlighted the complex interactions between urban elements and the
46 regional climate which resulted in numerical simulations preferred as an ideal tool to conduct urban
47 thermal related assessment in all scales.

48

49 In 2012, a simplified two-dimensional mathematical model was developed in order to simulate air
50 based UHI effect on two urban configurations: surface with two building rows and a surface with no-
51 building. The study highlighted the relation of UHI existence with the canyon aspect ratio; based on
52 building height, H against the width between the building facades, W [5]. This ratio was included for
53 the assessment of various urban air temperature and climatic studies [6]. Several studies have utilised
54 fixed aspect ratio for analysis [7] but investigation on asymmetrical aspect ratios were also carried out
55 [8]. Simulation of an urban configuration requires high effort to match with the realistic urban
56 environment due to asymmetrical height of the buildings. Several researchers suggested to simplify
57 the geometry patterns particularly by standardising the height of all simulated buildings [9]. Study of
58 [10] has simulated multiple canyon geometry for comparative analysis but still retained the canyon
59 aspect ratio in one particular standard.

60

61 The dynamic effects of the combination of solar heating and ambient wind speed in an urban canyon
62 were investigated by [7]. The work highlighted that poor ventilation was observed within street
63 canyon area as compared to the outside. It was mentioned in the published work of [2] that ground
64 heating was observed to have an influence on the wind speed and the temperature at lower levels but
65 with higher temperature facades of buildings, the buoyancy effect had more significant impact on the
66 canyon air patterns [9]. Furthermore, there was an evidence of heat accumulation alongside the
67 leeward wall as compared to the windward wall due to incapability of the air to dissipate the excessive
68 heat away from the wall [1]. It was mentioned by [3] that the surface temperatures of an urban scale
69 3D street canyon were unevenly distributed caused by the surface interaction to store, absorb and
70 release heat from the heat sources i.e. solar radiation and airflow from all axis. The thermal instability
71 that was caused by canyon air circulations has largely influence the pollution dispersion within street
72 canyons. In the study of [4], another factor which contribute to the UHI effect is the low turbulent

73 heat transport within street areas. This was observed when the streets were positioned perpendicular to
74 the predominant wind direction, which reduces the ventilation cooling effect and subsequently
75 reduces the heat release from surfaces. Therefore, high urban surface temperatures were noticed
76 within the areas with low-access to wind velocity. In the study of [11], findings suggested that ground
77 surface temperature was more sensitive to the variation of street canyon aspect ratio (H/W) during the
78 night time and vice-versa for the wall temperature. Although it was mentioned that the increase in the
79 aspect ratio could reduce the penetration of direct solar radiation, it should also be noted that the wall
80 temperature increases with the decreasing convective cooling. In the afternoon, average wall
81 temperature was higher due to increasing ground surface. By increasing longwave radiation, the walls
82 opposite to the isolated walls were found warmer than the shaded walls.

83

84 According to [12]; it is assumed that the flow field in the urban area modelling is generated mainly
85 based on the atmospheric motions. Computational Fluid Dynamics (CFD) can be utilised to
86 investigate the dynamics of heat environment to determine temperature distribution, UHI effect and
87 measurements on other aspect for urban planning. The CFD software allows to simulate the model in
88 full scale configuration (1:1) based on the actual urban measurements [13]. In addition, to model
89 passive energy design to achieve optimal thermal comfort, numerical methods such as CFD was also
90 mentioned to be acceptable for its use due to its capability to parameterise extensive boundary
91 conditions [14]. Overall, it is agreed that CFD modelling can provide higher resolution results and has
92 a lot potential for many thermal related studies [15].

93

94 Additional option in reducing computational uncertainty is by validating CFD analysis with
95 experimental data which is highly important to satisfy the quality assurance of the conducted
96 numerical analysis [4]. Overview of CFD validation studies were listed in [4] and it was highlighted
97 that more validation was conducted for microscale non-specific urban setting rather than for real
98 urban setting. In recent, a review by [16] on CFD development and application suggested that a
99 number of published papers without validation has slightly increased. This suggested that in some
100 research, accuracy is unnecessary for the main study objective. It was objected by [17] which
101 highlighted that although CFD has the ability to predict the modification of urban air velocity for
102 investigating air dispersion, testing and validation procedures are also required and are as important as
103 the modelling setup. It should be noted that previous researches on urban modelling were carried out
104 by multidisciplinary approaches i.e. flow patterns across buildings [18] but it is worth to mention that
105 most of the street canyon domain model was carefully developed based on COST Action 732 Best
106 Practice Guideline (BPG) for CFD Simulation of Flows in the Urban Environment [19].

107

108

109

110 **2.0 Previous work: Road pavement solar collector as urban heating mitigation technique**

111 Mitigation technology such as hydronic road pavement solar collector (RPSC) system was earlier
112 proposed to reduce the absorbed temperature of road surface by flowing medium, which allows heat
113 to be transferred from surface to bottom layers until it reaches the water pipes. In 1990s, outdoor
114 measurement analysis has found the potential of asphaltic and dark type of pavement to intensify the
115 thermal impact of outdoor environment due to excessive heat absorption as compared to the other
116 tested materials, see the published work of [20]. Two decades later, the concern was not only the heat
117 absorption but also regarding the underestimation of heat convection coefficient used during testing
118 which caused an overestimated surface temperature values i.e. wind speed and temperature [21]. the
119 observation of [22] also found an extremely high surface temperature during summer days, heat
120 dissipation technologies for asphalt pavements were proposed with purpose to reduce air and surface
121 temperature effects within urban environment [23]. In 2010, Asphalt Solar Collector (ASC) system
122 which allows heat dissipation from the road surface by using a cooling medium was proposed while
123 the absorbed heat was utilised for urban energy harnessing [24]. Concrete Solar Collectors (CSC) was
124 proposed and developed for material thermal enhancement [25]. In 2013, using multi-layered
125 pavement with higher porosity was preferred against the use of water pipe network due to improve
126 system thermal efficiency for renewable energy and UHI mitigation. The system seems promising
127 with the presented prototype with 75.0-95.0 % efficiency but it also experienced issues such as low
128 flow rates in the heat transfer of water medium across the porous pavement layer [26].

129

130 In this study, other types of solar collector technology were also reviewed, expanding the knowledge
131 of each of the system performance for urban application. In 2012, a review of Massive Solar-Thermal
132 Collectors (MSTC) highlighted the application of MSTC in three categories: (i) detached MSTC
133 application from building envelope i.e. pavement or prefabricated structures, (ii) partially integrated
134 MSTC via glazed and unglazed panels; and (iii) building integrated MSTC via building facade [27]. It
135 was mentioned that the application of heat pump to exchange thermal energy with the ground
136 encourages to use renewable source of low-enthalpy geothermal energy for heating and cooling
137 buildings [28]. In the study, grouting materials used for the sealer of the buried pipe were investigated
138 for the system thermal conductivity; demonstrating that natural and recycled aggregates provided an
139 ideal thermal optimisation. An investigation by [29] studied the mechanism of critical free-area ratio
140 (CFR) and its influencing factors using a simplified theoretical model to describe the heat and mass
141 transfer process on pavement. Numerical investigation of inlet-outlet temperatures from water-in-
142 glass evacuated tube solar collector has found the necessity to obtain an optimum inlet-outlet
143 temperature difference for optimum performance in thermal gain as well as to achieve less percentage
144 error in validating experimental setup [30]. In the study of [31], the system efficiency and deficiency
145 of a solar water heating system with evacuated tube collector and active circulation were investigated;
146 demonstrating the reduction in the system efficiency with the increase in the water temperatures. This

147 study highlighted the importance of the annual based analysis in determining the feasibility of the
148 system for hot water supply systems.

149

150 Apart from the evaluation of solar collector systems based on its design parameters, the study of [32]
151 highlighted the importance of investigating the system performance based on a number of outdoor
152 parameters i.e. solar irradiation, wind speed, air temperature. From the urban-rural comparative
153 analysis, it was concluded that weather condition according to time and location and urban
154 characteristics (built form, topology) had a significant influence on the system performance
155 efficiency. In 2015, the published work of [33] carried out CFD modelling of integrating the RPSC
156 system with simplified urban canyon (two building rows) and to be compared with the integrated
157 system with flat surface (no building canyon), as an alternative of evaluating the system in a near-to-
158 realistic event of UHI effect. Results have highlighted a significant unevenness in the temperature of
159 the canyon road surface as compared to the flat surface, thus has increased the performance of RPSC
160 in term of Potential Temperature Collection (PTC) and Surface Temperature Reduction (STR).
161 Further investigation was carried out on the optimisation of RPSC via four designated parameters
162 (inlet water velocity, water temperature, pipe depth and pipe diameter) within the two scenarios. The
163 remark of the study was on the comparative analysis of the RPSC performance for urban application
164 and rural application using the best condition of the system in obtaining optimum PTC and STR and
165 conversely for the worst condition of the system [34].

166

167 **2.1 Aim and objectives**

168 This study builds on previous researches of urban RSPC system [33] and investigates the potential
169 impact of modifying the shape of buildings from symmetrical [9] to asymmetrical form on the RPSC.
170 The relevant of this study is based on the complex urban environment that consists of various types of
171 topology in regards of the form, height or layout. In the earlier investigation, the urban configuration
172 used in this work consisted of two building rows with symmetrical height with one road in between
173 and the length of the street canyon was designed to be perpendicular to the direction of the airflow.
174 The current evaluation includes the comparison of the street canyon in symmetrical height to the street
175 canyon in asymmetrical height in two types which consists of: (i) the approaching building row has
176 higher height as compared to the second building row, and (ii) the approaching building row has
177 lower height as compared to the second building row. Based on these comparisons, this study aims to
178 estimate the PTC and STR in % of the RPSC system for each of the configuration and discussion
179 were made further to the previous designated works. Further explanation on the research method is
180 detailed in Section 3.

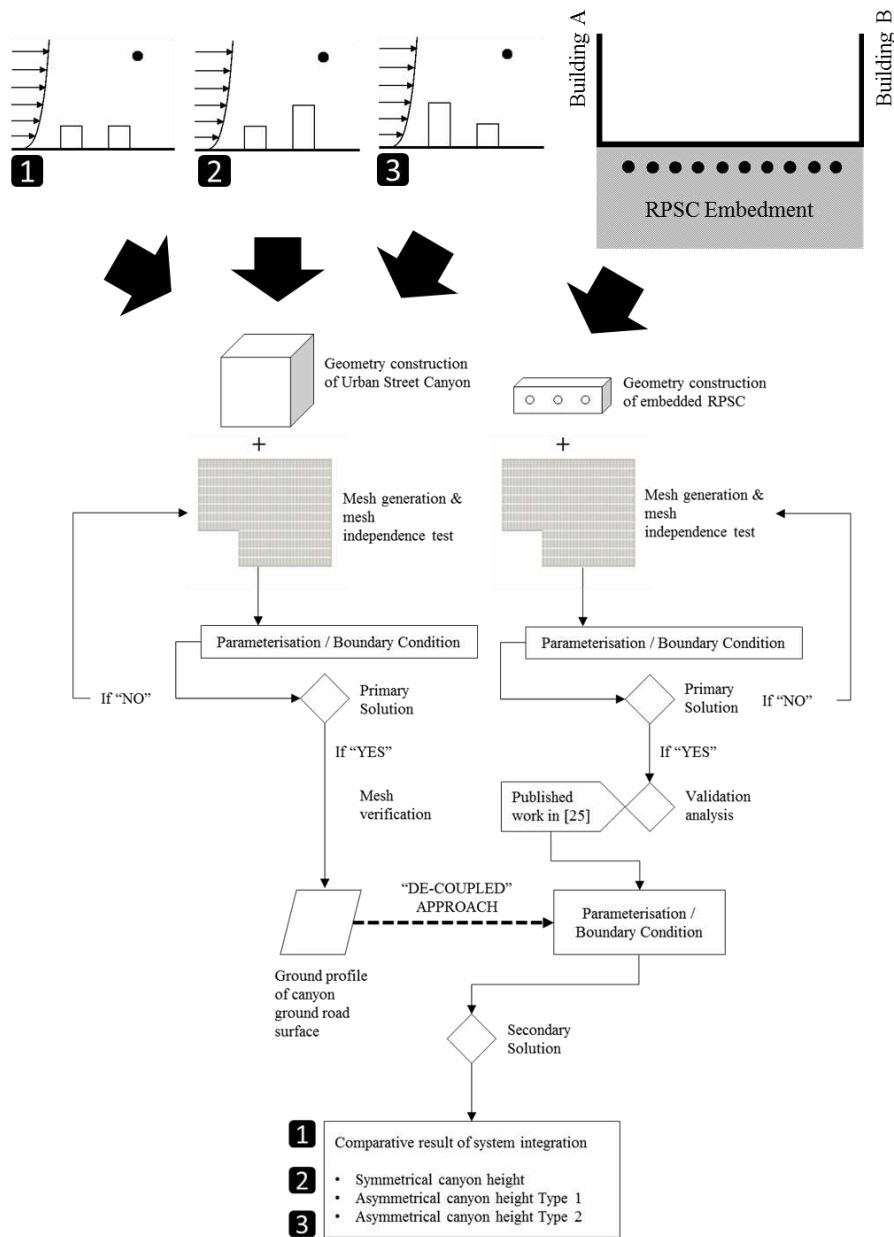
181

182

183

184 **3.0 Methods: De-coupled computational modelling**

185 Continuing from the previous study [33], a de-coupled computational modelling was proposed to
 186 evaluate and compare the effect of symmetrical street canyon height and two types of asymmetrical
 187 street canyon heights on RPSC system which was embedded in between two building rows. The de-
 188 coupled modelling approach means two separated domains were combined after the simulation results
 189 of primary domain (macro) which represents an outdoor urban environment above road surface were
 190 exported to the secondary domain (micro) which represents a simplified pipe embedment within road
 191 pavement layer. Figure 1 shows the study method chart of the proposed de-coupled CFD approach.
 192

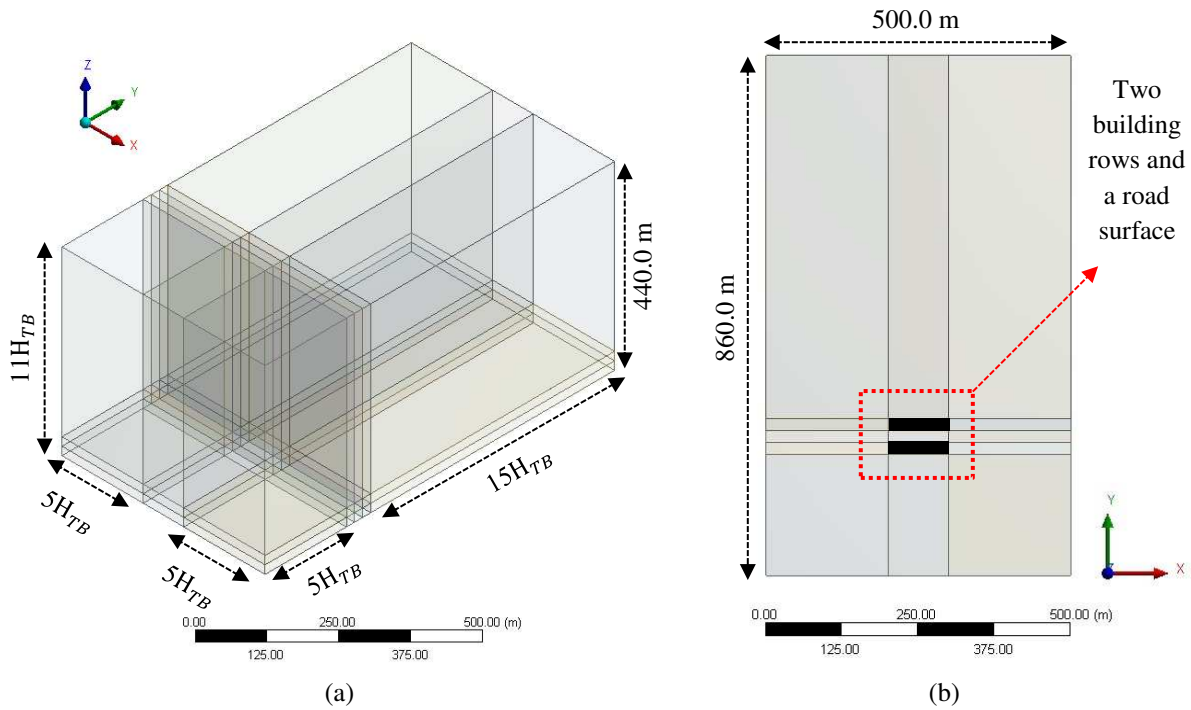


193 Figure 1: Method chart of de-coupled approach CFD model combining
 194 macro domain and micro domain

195 **3.1 Macro domain: geometry and mesh description**

196 A fluid flow domain was built representing an urban environment above road surface with size 860.0
 197 m length \times 500.0 m width \times 440.0 m total height in overall including two elongated building rows
 198 which were separated by 20.0 m width road surface in between. An inlet plane was determined to be
 199 5H away from the first approaching building wall, to be named Windward Wall 1 of Building A,
 200 meanwhile an outlet plane was determined to be 15H away from the second wall of the second
 201 building, to be named Leeward Wall 2 of Building B; see Figure 2.

202



203 Figure 2: Geometry domain and description in (a) 3D perspective (b) top plan

204

205 The height of the fluid domain was determined as 11H. The size of fluid flow has followed the
 206 recommendation of domain blockage ratio to be not more than 3.0 % [19]. An elongated street canyon
 207 with two symmetrical building rows with the dimension 100.0 m length \times 20.0 m width \times 20.0 m
 208 height (H) was compared to two types of asymmetrical elongated street canyons: (i) the first
 209 approaching building row has the height which was half the second approaching row (ii) the first
 210 approaching building row has the height which was double the second building row. This means the
 211 shortest building height, H_{SB} was set 20.0 m and the tallest building height, H_{TB} was set 40.0 m. To
 212 standardise the size of the fluid flow domain for all three models, the reference height (H) has to
 213 consider the tallest building height, H_{TB} ; thus $H = H_{TB}$. In addition, the analysis considered the
 214 building length of all domains to be perpendicular to the inlet airflow direction (in y axis). The first
 215 approaching wall acted as an obstacle to the airflow which encourage the airflow turbulent
 216 development in the afterward until it reaches the outlet plane.

217 3.1.1 Mesh setting

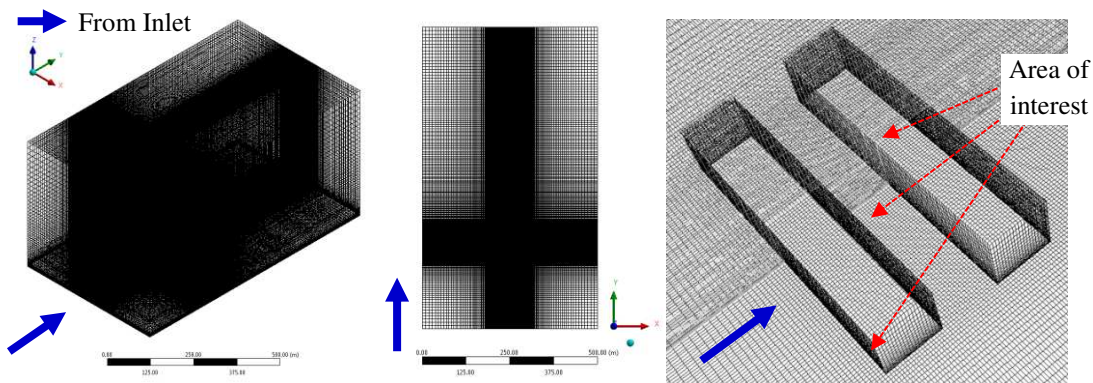
218 Full structured mesh was set for overall macro domain emphasising finer grids at the area of interest;
 219 building rows and street canyon surface. For the aforementioned setting; body slicing technique was
 220 carried out, dividing the domain into 45 sub bodies including building volumes. Subsequently, all
 221 body volumes were subtracted so that the interior of the buildings can be excluded from the boundary
 222 condition. The first cell height in all sub-volumes can be set similar 0.25 m based on edge sizing;
 223 generating more than 3 rows of cell above the first cell height before reaching 2.0 m pedestrian level
 224 as recommended by [35]. Full application of edge sizing with hard behaviour and bias setting was
 225 done on all sub bodies; see full description in Table 1 and generated mesh in three settings in Figure
 226 3. Mesh verification was carried out comparing the macro domain with generated cells in coarse,
 227 medium and fine setting.

228

229 Table 1: Mesh setting based on edge sizing

Solution	Coarse mesh	Medium mesh	Fine mesh
Edge sizing on macro domain			
Length between inlet and Windward Wall 1 Building A ($5H_{TB}$) on x axis (m)	4.5 with bias factor 10	4.0 with bias factor 10	3.5 with bias factor 10
Length between inlet and Leeward Wall 2 Building B ($15H_{TB}$) on x axis (m)	4.5 with bias factor 10	4.0 with bias factor 10	3.5 with bias factor 10
Width between symmetrical wall and building edge walls ($5H_{TB}$) on y axis (m)	4.5 with bias factor 10	4.0 with bias factor 10	3.5 with bias factor 10
Up to 20.0 m above building height (H_{TB}) (m)	4.5 with bias factor 2	4.0 with bias factor 2	3.5 with bias factor 2
40.0 m above ground level to symmetry boundary wall ($10H_{TB}$) (m)	13.0 with bias factor 4	12.0 with bias factor 4	10.0 with bias factor 4
Edge sizing on building rows			
Length on x axis (m)	1.15	1.0	0.85
Width on y axis (m)	1.15	1.0	0.85
Building height (H_{TB}) on z axis (m)	1.15 with bias factor 10	1.0 with bias factor 10	0.85 with bias factor 10
Cell information			
Total cell (nos)	2,170,638	2,988,000	4,810,824
Total node (nos)	2,238,228	3,072,420	4,926,387

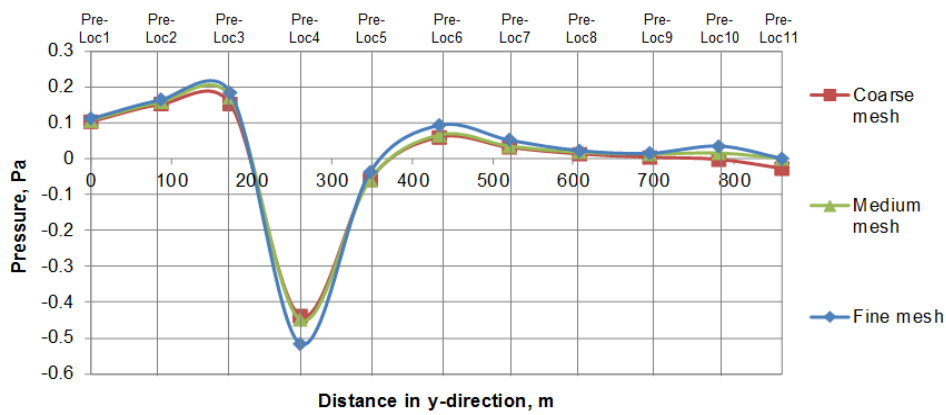
230



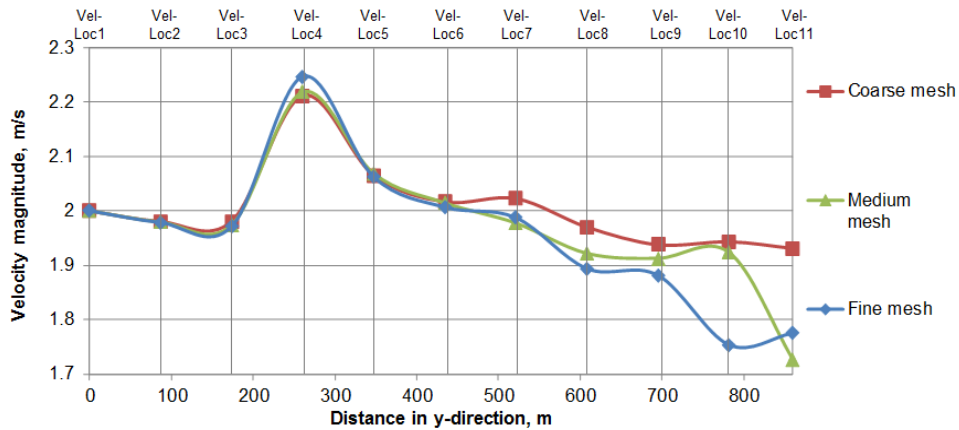
231 Figure 3: Full-structured mesh generated for macro domains comparing symmetrical and asymmetrical canyon
 232 height with cell refinement concentrated on area of interest

233 3.1.2 Mesh verification

234 To verify that the macro domain simulation was independent from the influence of grid sizing and cell
 235 number, air pressure and air velocity magnitude were plotted in 11 points across the macro domain (in
 236 y axis) above 60.0 m from the ground level (0.0 m) comparing coarse, medium and fine meshes.
 237 Based on Figure 4(a), graph trend of all meshes were comparable except for nominal higher values
 238 plotted for 7 out of 11 points in fine mesh as compared to the other two meshes. In Figure 4(b), the
 239 graph trend can be mentioned comparable for all meshes between Location 1 (Loc1) to Location 6
 240 (Loc6) as it was observed that the obtained gap was between 0.5-2.0 m/s to compare the values
 241 afterward. However, velocity in all meshes seems decelerated when reaching outlet plane (Loc11).
 242



(a)



(b)

243 Figure 4: Mesh verification test plotted on 11 points comparing (a) air pressure (b) air velocity

244

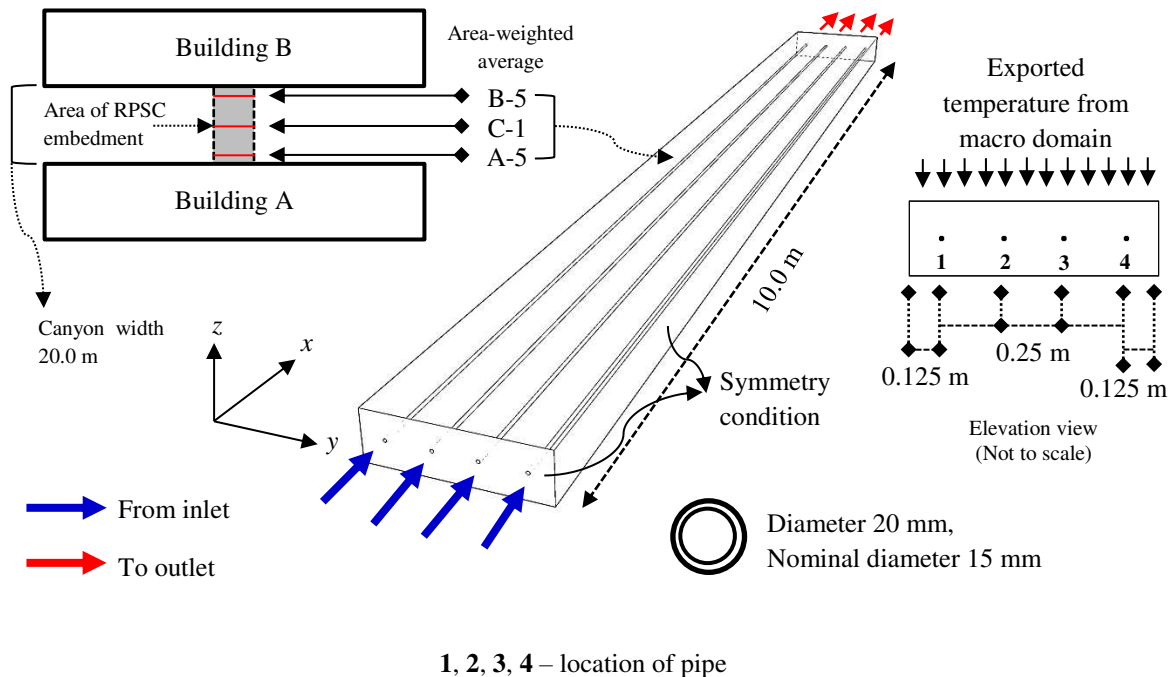
245 Based on the verification results, medium mesh was selected as the optimum mesh for the analysis as
 246 it shows comparable trend with the coarse mesh fine mesh while also reducing computational power
 247 requirement up to 40.0 % as compared to fine mesh.

248

249

250 **3.2 Micro domain: geometry and mesh description**

251 It should be noted that based on the previous related work [33], RPSC system was layered underneath
 252 road surface within street canyon. In this study, RPSC pipes were assumed parallel to the length of the
 253 building rows approximately within the 10.0 % area of the total ground road surface for
 254 simplification. 4 nos 20 mm diameter RPSC pipes were designed to be embedded 0.15 m (150 mm)
 255 underneath road surface with the dimension 10.0 m length, $L \times 1.0$ m width, $W \times 0.3$ m (300 mm)
 256 depth, D ; see Figure 5. The gap between the pipes was set 0.25 m (250 mm). As referred to the
 257 previous setting [33], three pipes were selected based on (i) the centre location, C; (ii) the pipe which
 258 the surface received highest temperature, A-5; and (iii) the pipe which the surface received lowest
 259 temperature, B-5. For simplifying the simulation, surface temperature within the area of 10.0 m \times 1.0
 260 m from the macro domain at the three aforementioned locations was exported for the boundary
 261 condition of the micro domain.
 262



263 Figure 5: Configuration of micro domain (RPSC system) consisting 4 nos straight pipe
 264

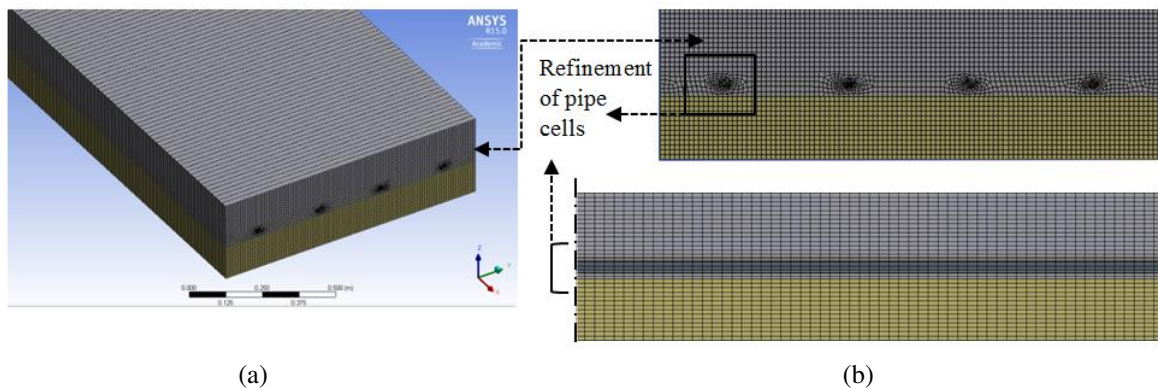
265 **3.2.1 Mesh setting**

266 Automated mesh was generated by sizing the edge of the pavement and pipe bodies; see Table 2
 267 below. The micro domain was divided into 1 pavement body and 4 pipe bodies. For the pavement
 268 body; three sub bodies were created, separating the embedment region of the pipes from the upper
 269 layer and the lower layer. Hard behaviour on the edge sizing was set in order to force the generated
 270 cells of all pavement bodies in major hexahedral form so that full structured mesh can be obtained.
 271 Subsequently, this behaviour has to influence the cells generated for the pipe body; see Figure 6.

272 Table 2: Mesh setting for grid independence analysis

Solution	Coarse mesh	Medium mesh	Fine mesh
Edge sizing on RPSC pavement and pipe bodies			
Length on <i>x</i> axis (m)	0.0250	0.02250	0.0200
Width on <i>y</i> axis (m)	0.0010	0.00975	0.0095
Thickness on <i>z</i> axis (m)	0.0010	0.00975	0.0095
Pipe length (m)	0.0250	0.02250	0.0200
Cell information			
Total cell (nos)	1,414,800	1,625,140	1,979,000
Total node (nos)	1,468,462	1,687,664	2,053,098

273



(a) (b)
Figure 6: Example of generated medium mesh for micro domain

274

275

276 3.2.2 Mesh validation of micro domain (pipe)

277 The mesh settings (coarse, medium and fine) were validated against small-scale laboratory pavement
 278 with coil pipe [36] on temperature distribution plotted across pavement layers. The inlet flow rate for
 279 all meshes was set 1757 mL/min (0.03 kg/s). As Figure 7, there were 15 points plotted across
 280 pavement depth, to be named Point 0 until Point 14. The pipe embedment for both setups (numerical
 281 and experimental) was located in the centre of pavement layer. In this study, the validation was
 282 carried out precisely at pipe 1 at the location 5.0 m away from the water inlet and 5.0 m away from
 283 the water outlet in *x* axis. Only at seventh point, the plot was obtained outside the body of Pipe 1
 284 following the published work of [36]; see Figure 7. Based on Figure 7, the error calculated for coarse
 285 mesh, medium mesh and fine mesh were on average 1.876 %, 1.874 % and 1.860 % respectively. Out
 286 of 15 points, Point 3 for all three mesh settings had obtained the highest error value, not more than 5.0
 287 %. The comparison between the three mesh settings suggested that the obtained temperatures at all
 288 points were grid independent from the mesh cells with insignificant variance comparing the obtained
 289 values location to location. Thus, this study chose to carry out further investigations with fine mesh
 290 setting.

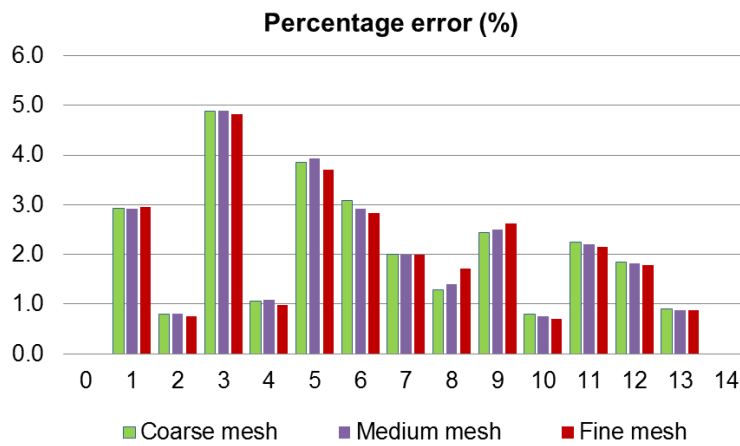
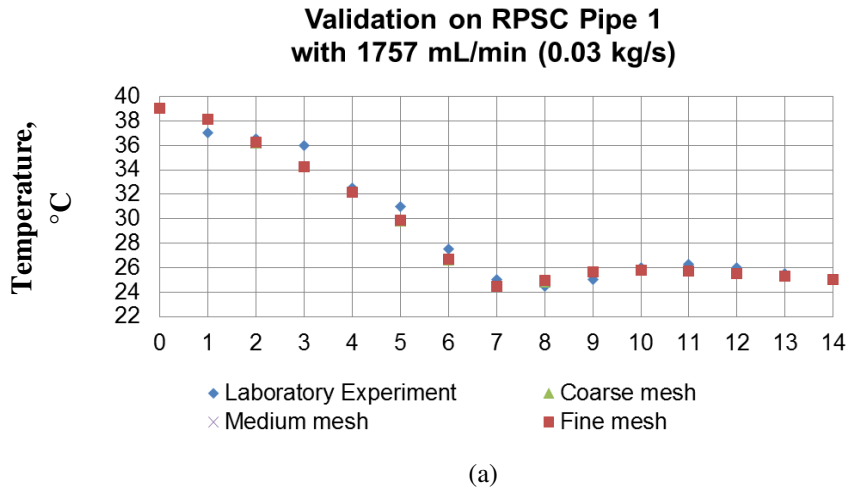


Figure 7: Verification of mesh and validation of temperatures across pavement layers
(a) mesh against laboratory results (b) percentage error, %

291
292
293
294
295
296
297
298
299
300
301
302
303
304
305
306

3.3 Boundary conditions

For all macro domains, location of the simulation was set following the setting of [7] in Milan urban centre, Italy with longitude 9.18°E, latitude 45.47°N and UTC +1. The simulation took the consideration of a hot day with less wind [37] which was during summer 21st June at 13:00 hour. The inlet air temperature was set 303 K (30°C) with a constant 2.0 m/s air velocity. The turbulence intensity was set as 10.0 % for assisting the turbulence development [9]. In this study, sand-grain roughness height k_s was 0.25 m and roughness constant C_s was set as default, 0.5. For RPSC pipes, 0.1 m/s water velocity was set based on the lowest range of velocity input following [34] with turbulence intensity set as 0.08819 % meanwhile the inlet water temperature was set as 293 K (20 °C). Extending from the previous work [33], boundary conditions applied for wall surfaces are shown as Table 3.

307 *Table 3: Boundary condition applied to wall surfaces*

Description	Surface description	Temperature K (°C)	Thickness (m)	Density (kg/m ³)	Specific heat (J/kg K)	Thermal conductivity (W/m K)	Emissivity
Validation against experiment work [36]	Pavement top surface	312 (39 °C)	NA	1000	1000	0.9	0.9
	Pavement bottom surface	298 (25 °C)	NA	1000	1000	0.9	0.9
Macro domain analysis [7]	Pavement	288	NA	1000	1000	0.9	0.9
Micro domain analysis [33]	Pavement	NA	NA	1000	1000	0.9	0.9
	Copper pipe [38]	NA	0.005 m (5 mm)	8978	381	387.6	0.9
	Water [38]	293 (20 °C)	NA	998.2	4182	0.6	NA

308

309 **3.4 Solution model**

310 For the simulation of three dimensional fluid flow and heat transfer within macro domain and between
 311 macro domain and micro domain, Finite Volume Method (FVM) combined with SIMPLE pressure-
 312 based solver in ANSYS Fluent 15.0 was selected. Effect of solar radiation on the area of interest
 313 requires using Solar Load model to load sunshine fraction on geometry based on locations (as
 314 mentioned in Section 3.3) coupled with Discrete Ordinate (DO) radiation model which treats all
 315 bodies as grey due to the emissivity of the materials. To simulate atmospheric boundary layer (ABL)
 316 in urban area; 3D pressure and steady Reynold Averaged Navier Stokes (RANS) with Standard k -
 317 epsilon ($k-\epsilon$) equation was used to solve turbulence development for high Reynold number [38]. This
 318 model was fully considered for its principle of momentum, continuity and heat conservation that used
 319 pressure and steady RANS equations meanwhile standard steady-state $k-\epsilon$ model assumes an airflow
 320 is fully turbulent based on transport equation for turbulence kinetic energy (k) and dissipation rate (ϵ)
 321 [33].

322

323 *3.4.1 Performance calculation in temperature collection and surface temperature reduction*

324 In calculating the potential temperature collection (PTC) and surface temperature reduction (STR),
 325 pipe water inlet temperature ($T_{w,i}$), water outlet temperature ($T_{w,o}$), surface temperature before pipe
 326 simulation ($T_{s,initial}$) and surface temperature after pipe simulation ($T_{s,final}$) are required. In
 327 obtaining $T_{s,final}$, the surface static temperature on the mirror side of the surface that was imposed
 328 with initial measured temperature, 150 mm below the pipe location (centre-to-centre) was obtained.
 329 Calculation of ΔT , PTC and STR are explained as Equation 1, 2 and 3 below:

330

331 ΔT (in °C) $= T_{w,o} - T_{w,i}$ (1)

332 Potential Thermal Collection, PTC (in °C) $= \Delta T / T_{w,i} \times 100.0 \%$ (2)

333 Surface Temperature Reduction, STR (in °C) $= (T_{s,initial} - T_{s,final}) / T_{s,initial} \times 100.0 \%$ (3)

334

335 **4.0 Results and discussion**

336 This section discusses the results comparing the temperature distribution of the canyon surface
337 between the three canyon settings (Section 4.1), sectional air velocity at the centre of the canyon
338 (Section 4.2), temperature effect on the building facades for symmetrical and asymmetrical settings
339 (Section 4.3) and analysis of RPSC performance based on PTC and STR in percentage (Section 4.4).

340

341 **4.1 Comparative analysis on temperature of canyon road surface**

342 Figure 8(a), 8(b) and 8(c) shows the surface temperature contour of elongated canyon road surface in
343 symmetrical canyon height, asymmetrical canyon height Type 1 and asymmetrical canyon height
344 Type 2; respectively. As the previous studies have highlighted regarding the orientation of solar
345 radiation on domain [33], it should be noted that the Building B of these three cases was in the
346 position which obstructed the nearby surfaces to obtain direct solar heat flux due to shadow effect and
347 subsequently reduced the temperature of the nearby road surface. Previous studies have highlighted
348 on the refraction of solar radiation towards the ground and facades of the Building A, caused
349 temperature to elevate at the particular surfaces. With the modification of the canyon height, it was
350 observed that its effect on surface temperature was significant. In Figure 8(a), lower surface
351 temperature was observed near the right and left canyon openings on x axis meanwhile higher
352 temperature was observed at the centre of the canyon, confirming the previous analysis of [33].

353

354

355

356

357

358

359

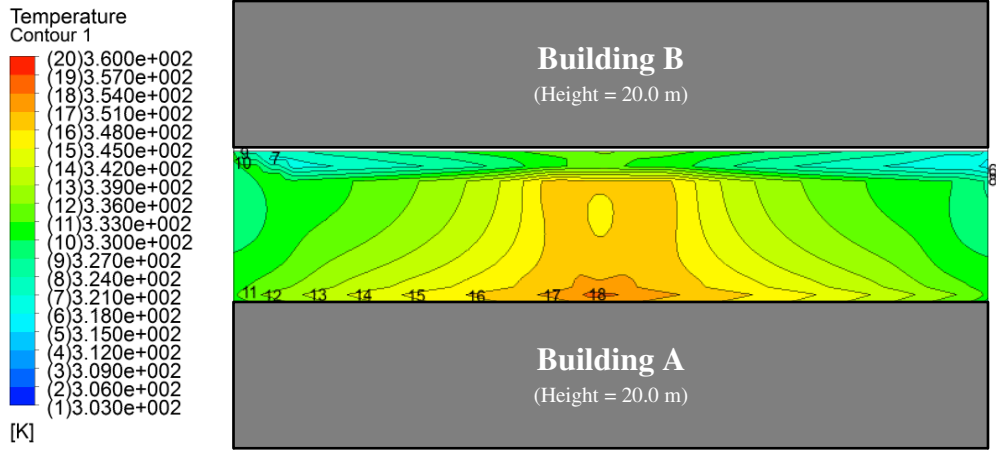
360

361

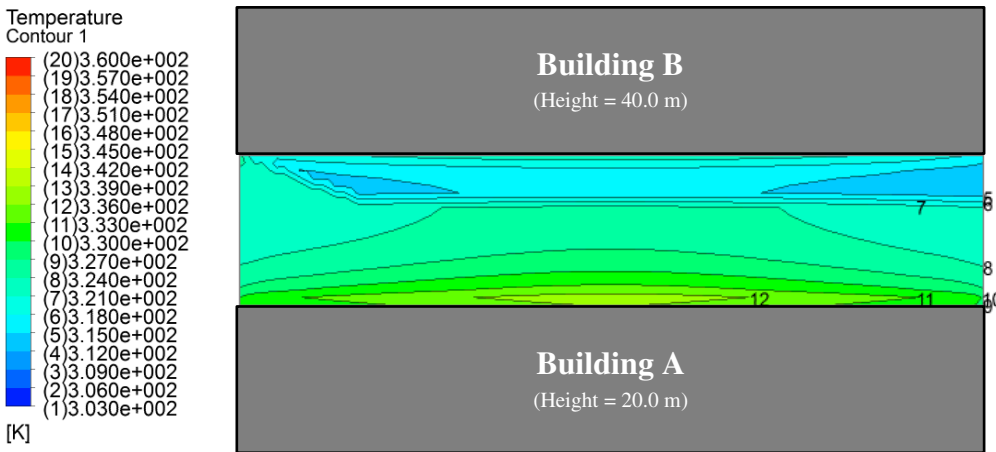
362

363

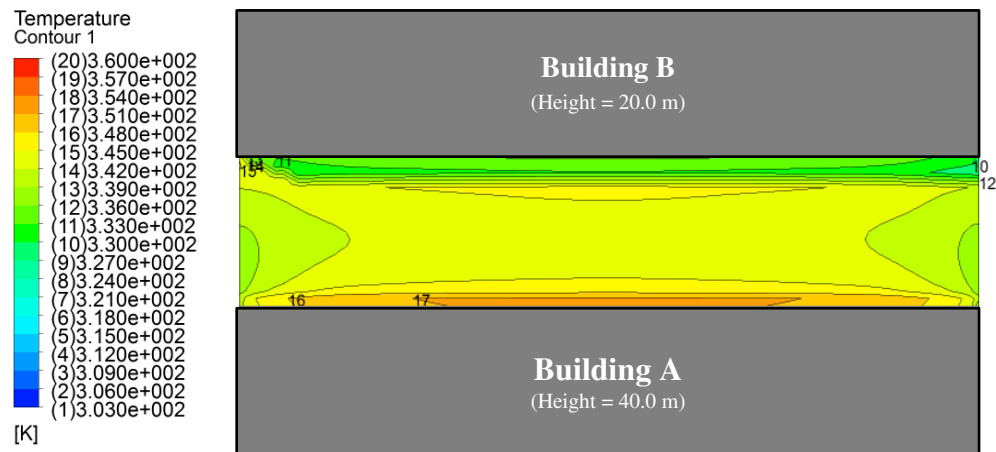
364



(a)



(b)



(c)

Figure 8: Temperature contour of canyon road surface comparing
 (a) Symmetrical canyon height (b) Asymmetrical canyon height Type 1
 (c) Asymmetrical canyon height Type 2

365
 366
 367
 368
 369

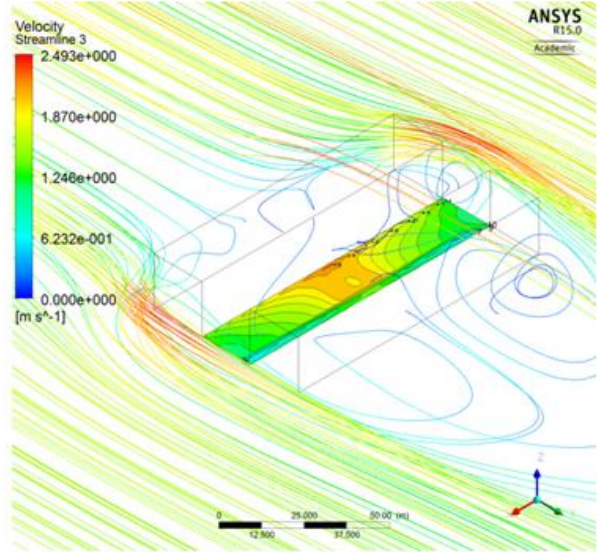
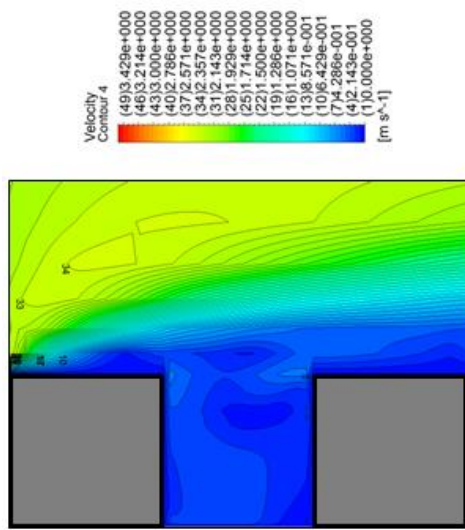
370 Result based on asymmetrical canyon height Type 1 as per Figure 8(b) provided significant difference
371 in trend. The Building B which was 20.0 m higher in height as compared to the Building A has caused
372 larger shadowed area on canyon road surface with much lower temperature as compared to the result
373 obtained with symmetrical canyon height. Refraction of solar radiation has occurred to the surface
374 close by the Building A, conforming to the solution setting. Based on the analysis with asymmetrical
375 canyon height Type 2 in Figure 8(c), it can be observed that the setting of lower building height on the
376 second row has caused a similar shadow effect on canyon road surface as the symmetrical canyon
377 height. However, the surface temperature at the centre towards right and left canyon openings was
378 observed to be identical with fewer contours due to a better distribution of the temperature. Similar to
379 the other canyon settings, the temperature of the canyon road surface close by the Building A obtained
380 highest temperature over other surface area. Further discussion was carried out in Section 4.2 from the
381 aspect of air velocity streamlines, which provided a clear explanation on the significant comparison in
382 canyon surface temperature when street canyon height was modified.

383

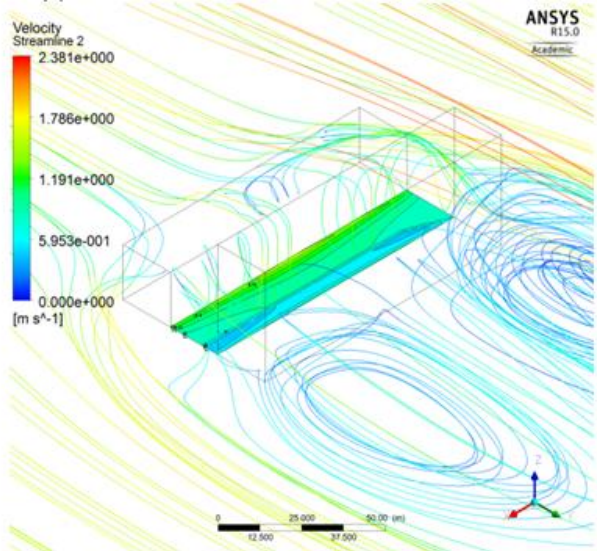
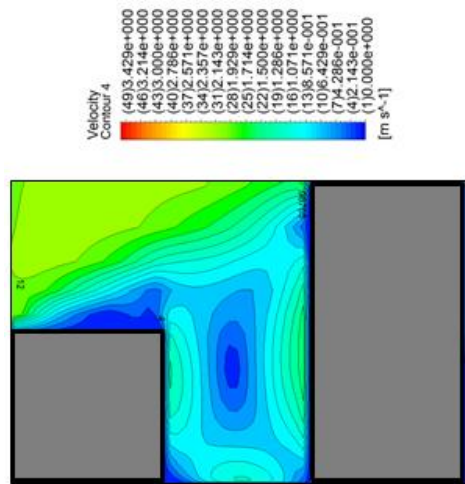
384 **4.2 Comparative analysis on air velocity streamlines**

385 3D air velocity streamlines were analysed with forward and backward effects in comparing the three
386 aforementioned street canyon settings; see Figure 9. Overall, the first façade wall (Leeward Wall 1)
387 has caused the airflow to cross over the street canyon and simultaneously to be dispersed to the
388 canyon edges in avoiding the vertical obstacle. Penetration of air from the canyon openings was
389 observed in all settings. However, with asymmetrical height, airflow movement was found to be
390 significantly modified. Based on Figure 9(b); it can be observed that the obstruction from the Building
391 B which has higher height has caused the swirling air directed down to the canyon road surface,
392 cooling the temperature of the surface. Simultaneously, the shadow of the Building B has increased
393 the cooling effect. With symmetrical canyon height setting as per Figure 9(a); swirling air was
394 observed more visible at the right and left openings, creating uneven temperature distribution from
395 low (closer the openings) to high (centre of street canyon). This effect was also combined with the
396 refraction of solar radiation on the surface with less shadows resulted in higher overall temperature as
397 compared to the asymmetrical canyon settings. Based on Figure 9(c), the obstructed Leeward Wall 1
398 of the Building A has caused larger swirling air passed over the Building B due to air movement
399 based on high to low pressure. It should be noted that the penetration of air from the canyon openings
400 (top, right and left) also occurred but with minimal effect on cooling the temperature of the canyon
401 road surface. This can be observed from the surface temperature contour classified at (15) or 345.0 K
402 has dominated approximately 60.0 % of the total surface area. Correlation between the street canyon
403 height and heat transfer from the solution model to the canyon road surface was further discussed in
404 Section 4.3. In this section, 3D analysis of the temperature of building facades facing street canyon
405 was carried out.

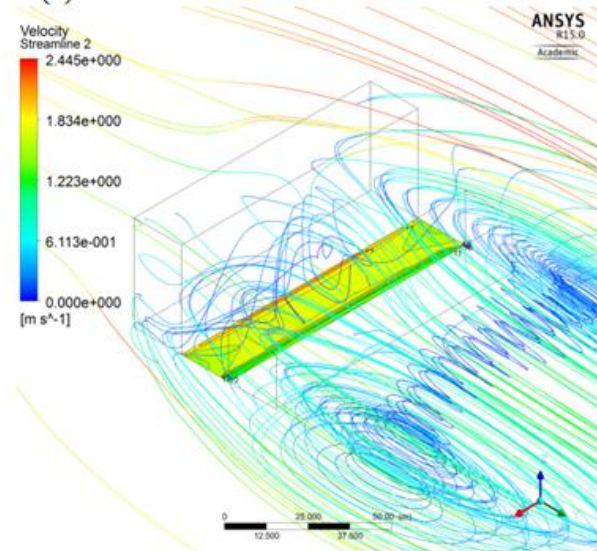
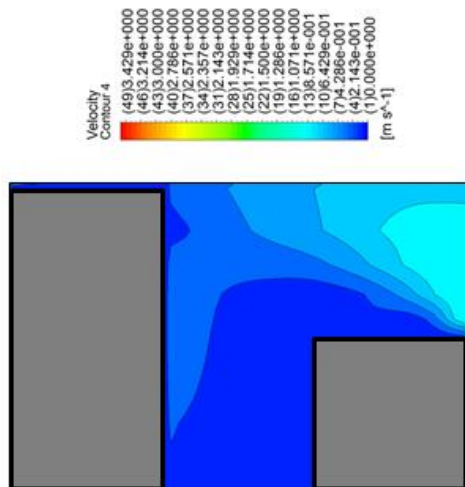
406



(a)



(b)



(c)

407

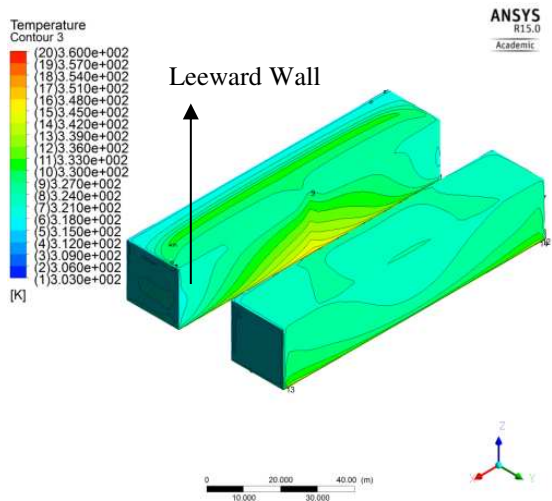
408

Figure 9: Air velocity streamlines comparing (a) Symmetrical canyon height (b) Asymmetrical canyon height Type 1 (c) Asymmetrical canyon height Type 2

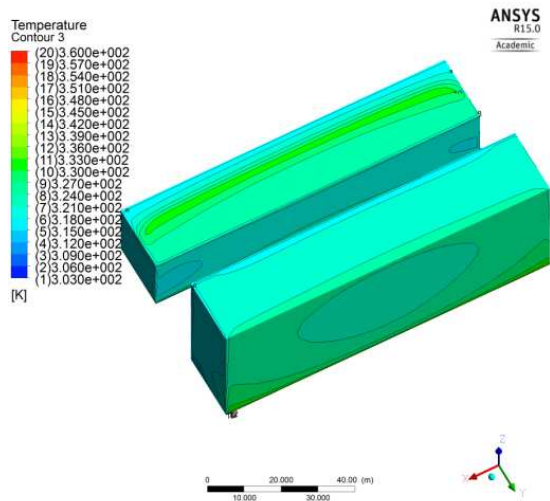
409 **4.3 Comparative analysis on façade temperature**

410 Figure 10 (a), 10(b) and 10(c) demonstrates the temperature contour of building facades facing street
411 canyon (Leeward Wall 1 for Building A and Windward Wall 1 for Building B) for symmetrical
412 canyon height, asymmetrical canyon height Type 1 and asymmetrical canyon height Type 2;
413 respectively. As shown in Figure 10, the temperature contour of all façades facing street canyon has
414 gradually increased according to the height. The closer to the ground, the higher the temperature was
415 obtained, depending on the fraction of solar radiation and the temperature of canyon road surface.
416 Based on Figure 10(a-i) and 10(a-ii), it can be observed that higher temperature contour was at the
417 centre of the facades closer to the road level; similarly followed the trend of canyon road surface. For
418 asymmetrical canyon height Type 1, the Windward Wall 2 (see Figure 10(b-i)) has double the façade
419 area as compared to other street canyon settings. As the obstruction to the airflow occurred, the
420 swirling air within the street canyon aided to reduce the temperature of the façade more than
421 Windward Wall 2 of other street canyon settings. As for the Leeward Wall 1 (see Figure 10(b-ii)), the
422 obstruction from the Building B in receiving direct solar radiation has shown that the façade has
423 obtained almost identical low temperature except for nominal temperature difference nearby the
424 canyon openings (right and left) and closer to the road level.

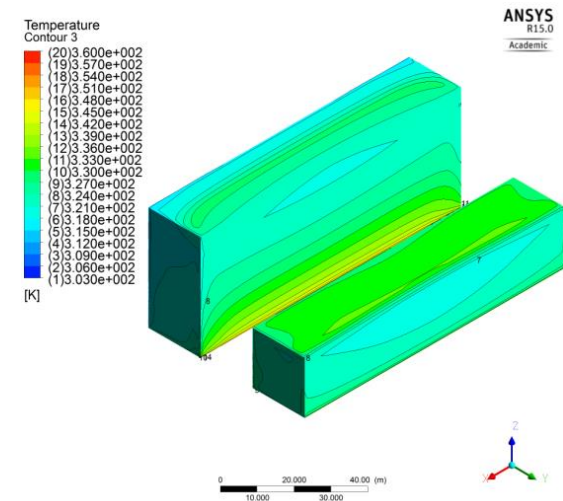
425
426 The temperature contour was observed to be in higher range (from ground level to rooftop level) with
427 almost identical temperature distribution from the right opening to the left opening for the Leeward
428 Wall 1 of asymmetrical canyon height Type 2; see Figure 10(c-i). Meanwhile for Windward Wall 2 as
429 per Figure 10(c-ii), almost 50.0 % of the surface area nearby the road level was observed with the
430 temperature contour classified at 14 or with 342.0 K. As mentioned in the previous section; the
431 increased height of the Building A over the Building B has caused large air swirl passed over the
432 Building B, reducing the penetration of airflow from the right and left canyon openings. Thus, the
433 temperature for Windward Wall 2 was observed to be almost identical end to end of the facades.



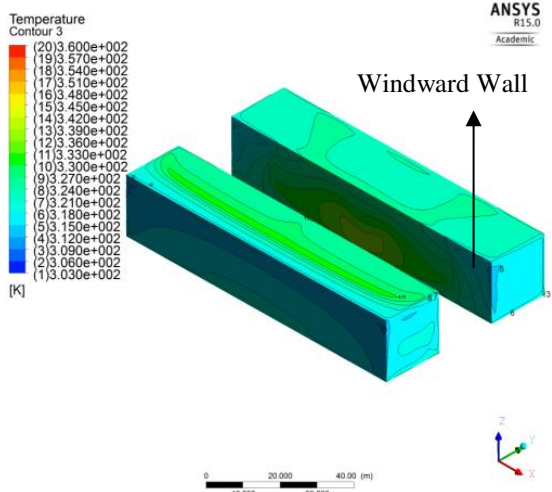
(a-i)



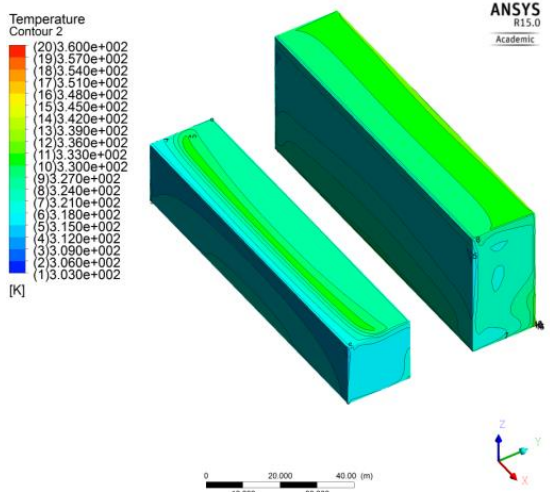
(b-i)



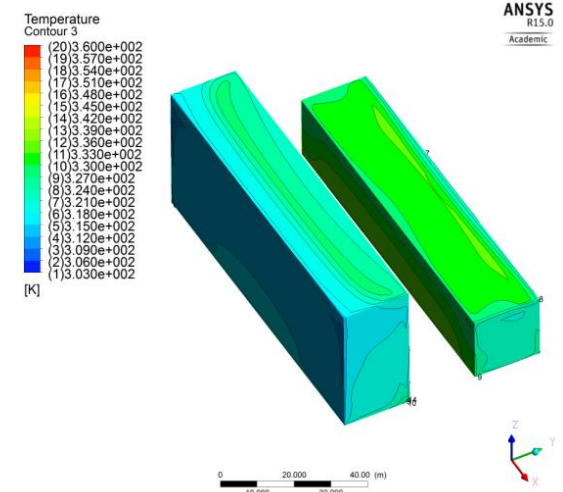
(c-i)



(a-ii)



(b-ii)



(c-ii)

Figure 10: Façade temperature comparing
 (a) Symmetrical canyon height – i & ii (b) Asymmetrical canyon height Type 1 – i & ii (c) Asymmetrical canyon height Type 2 – i & ii

434
 435

436 **4.4 System performance based on macro domain**

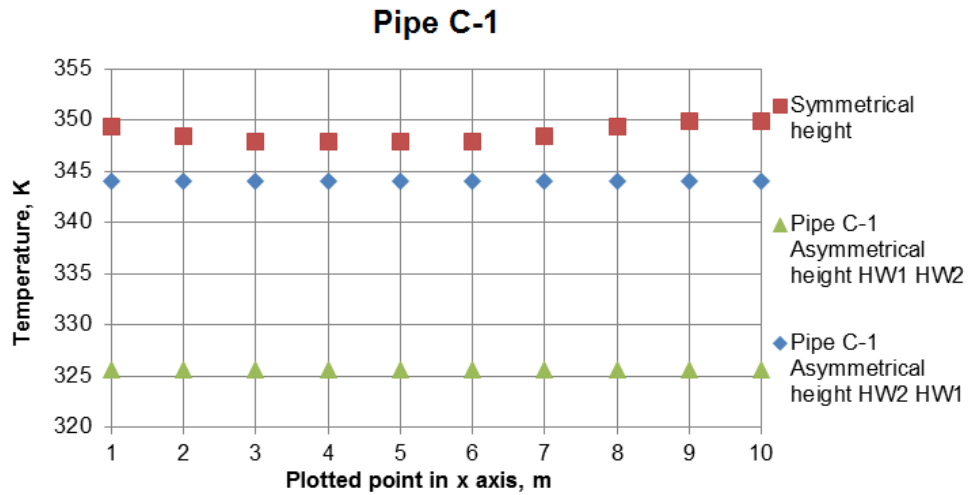
437 This section discusses the results of the RPSC system simulation that utilised the values of average
 438 surface temperature imported from the simulation of macro domain. As mentioned in Section 3.2,
 439 three locations were selected based on: (i) the centre location, C; (ii) the surface that received highest
 440 temperature, A-5; and (iii) the surface that received lowest temperature, B-5. Figure 11 demonstrates
 441 the comparative results of 10 temperature points plotted from the canyon surface between the location
 442 245 m and the location 255 m in x axis. Based on the results; it was observed that the symmetrical
 443 canyon height has caused canyon road surface to obtain higher temperature for location C and A-5 by
 444 25.21-43.93 % and 3.15-6.51 % than the asymmetrical canyon height Type 1 and asymmetrical
 445 canyon height Type 2, respectively. For location B-5, it was observed that the surface within the
 446 asymmetrical canyon height Type 2 has obtained 0.31 % surface temperature higher than the
 447 symmetrical canyon height. Meanwhile, the surface within the asymmetrical canyon height Type 1
 448 has obtained the lowest temperature; 20.14-23.08 % behind the other two canyon settings. Based on
 449 the plotted points, an average temperature of $T_{s,initial}$ was calculated and to be set as the boundary
 450 condition for the micro domain. The final temperature $T_{s,final}$ was then obtained to calculate STR in
 451 %; see Table 4.

452

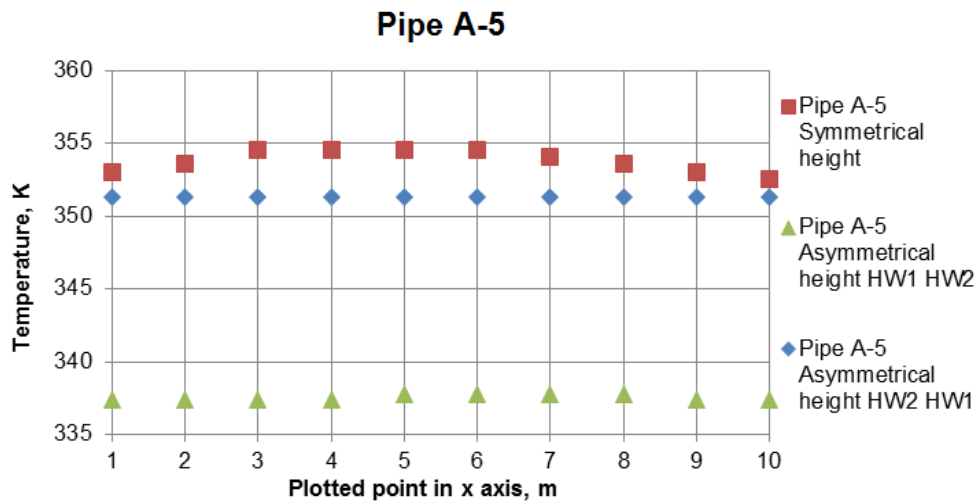
453 *Table 4: Calculation of average surface temperature according to locations*

Plot No	Pipe B-5			Pipe C-1			Pipe A-5		
	SCH	AC1	AC2	SCH	AC1	AC2	SCH	AC1	AC2
Point_1	333.32	319.88	333.84	349.39	344.04	344.04	353.02	337.36	351.32
Point_2	333.84	319.88	333.84	348.35	344.04	344.04	353.53	337.36	351.32
Point_3	334.36	319.88	334.33	347.83	344.04	344.04	354.57	337.36	351.32
Point_4	334.88	319.88	334.33	347.83	344.04	344.04	354.57	337.36	351.32
Point_5	334.87	319.88	334.33	347.83	344.04	344.04	354.57	337.77	351.32
Point_6	334.87	319.88	334.33	347.83	344.04	344.04	354.57	337.77	351.32
Point_7	333.84	319.88	334.33	348.35	344.04	344.04	354.05	337.77	351.32
Point_8	333.32	319.88	334.33	349.39	344.04	344.04	353.53	337.77	351.32
Point_9	333.32	319.88	333.84	349.91	344.04	344.04	353.02	337.36	351.32
Point_10	332.80	319.88	333.84	349.91	344.04	344.04	352.50	337.36	351.32
Average $T_{s,initial}$, K	333.94	319.88	334.13	348.66	344.04	344.04	353.79	337.52	351.32
Average $T_{s,final}$, K	308.18	302.97	308.25	313.64	305.08	311.93	315.55	309.51	314.63

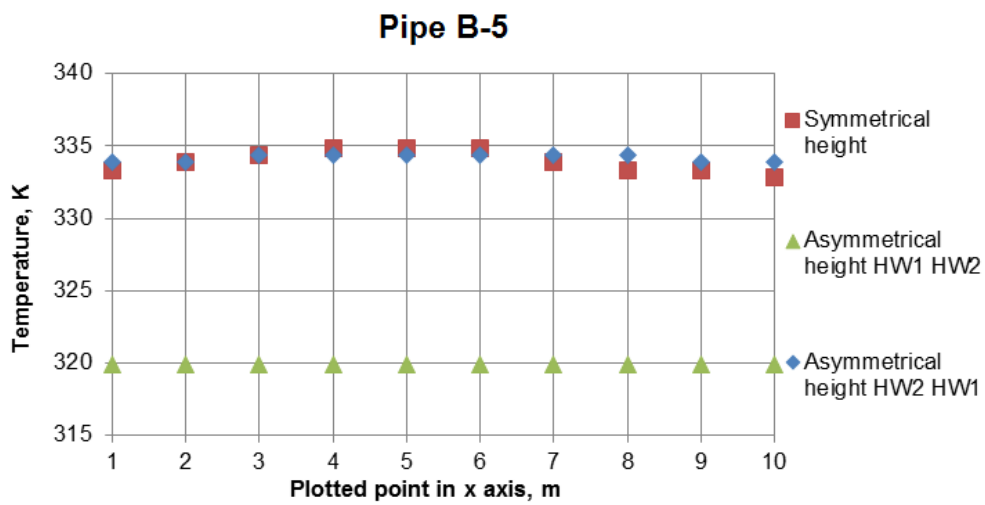
SCH = Symmetrical Canyon Height, AC1 = Asymmetrical Canyon Height Type 1, AC2 = Asymmetrical Canyon Height Type 2



(a)



(b)



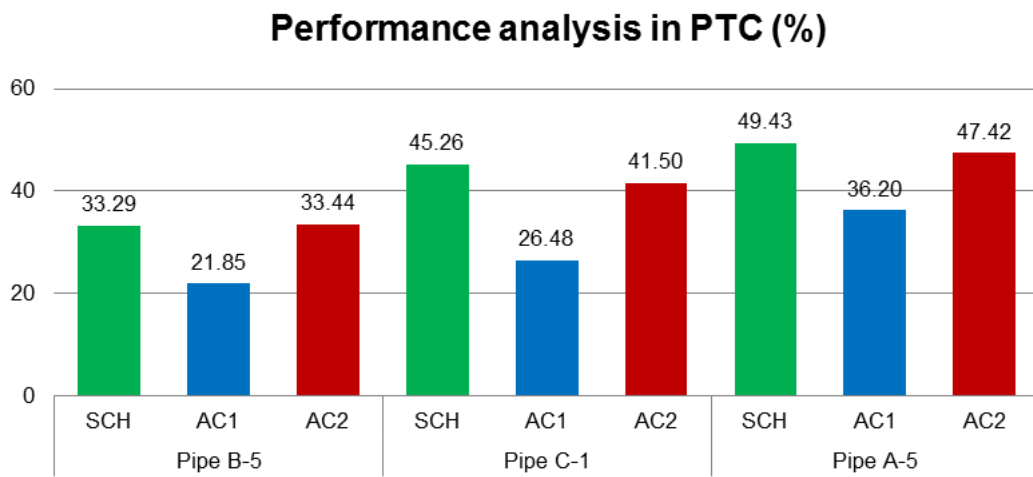
(c)

Figure 11: Surface temperature values plotted on 10 points comparing (a) Symmetrical canyon height (b) Asymmetrical canyon height Type 1 (c) Asymmetrical canyon height Type 2

454
455
456

457 4.4.1 Potential temperature collection in percentage, %

458 Figure 12 compares the potential temperature collection (PTC) in % based on the temperature
 459 difference between the outlet water temperature and the inlet water temperature (*Delta T*) of the RPSC
 460 system. It was observed that in overall, the PTC values during hot summer day were not less than 20.0
 461 % and not more than 50.0 %. At all locations where the comparison was based on the street canyon
 462 configuration in Figure 12; it was found that the highest PTC values obtained by symmetrical canyon
 463 height were 53.26 % and 4.58 % more than the asymmetrical canyon height Type 1 and the
 464 asymmetrical canyon height Type 2, respectively.
 465



SCH = Symmetrical Canyon Height, AC1 = Asymmetrical Canyon Height Type 1, AC2 = Asymmetrical Canyon Height Type 2

Figure 12: Potential Temperature Collection (PTC) in %

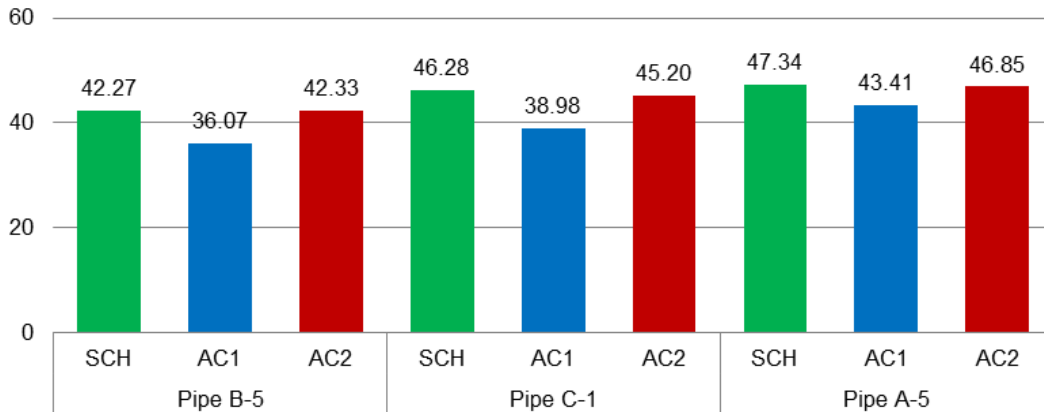
466
467

468 4.4.2 Surface temperature reduction in percentage, %

469 Based on Figure 13, it can be observed that surface temperature reduction (STR) for all canyon
 470 configurations were not less than 35.0 % and not more than 50.0 %. significant difference in values
 471 were found when comparing the asymmetrical canyon height Type 1 and the other two canyon
 472 settings, which was on average 15.0 % less in the STR performance. Insignificant difference can be
 473 found when comparing the symmetrical canyon height and asymmetrical canyon height Type 2,
 474 which was on average 1.2 %. For the location B-5 where the RPSC pipes B-5 were located, it should
 475 be highlighted that both PTC and STR values based on the simulation of asymmetrical canyon height
 476 Type 2 have dominated the PTC and STR values based on the simulation of symmetrical canyon
 477 height by 0.15 %.

478
479
480

Performance analysis in STR (%)



SCH = Symmetrical Canyon Height, AC1 = Asymmetrical Canyon Height Type 1, AC2 = Asymmetrical Canyon Height Type 2

Figure 13: Surface Temperature Reduction (PTC) in %

481

482

483 5.0 Conclusions and future work

484 This study evaluated the effect of the urban form on canyon road surface and on the performance of

485 the RPSC system which highlighted the modification of height in building rows under three settings:

486 (i) symmetrical canyon height, (ii) asymmetrical canyon height Type 1 – the height of first

487 approaching building row is shorter than the second building row, and (iii) asymmetrical canyon

488 height Type 2 – the height of first approaching building row is taller than the second building row.

489 Several conclusions were made:

490

491 (i) Temperature contours of canyon road surface for symmetrical canyon height had shown

492 that the direction of colder to hotter spots was from the canyon openings (right and left)

493 toward the centre of the surface area meanwhile from the simulation of asymmetrical

494 canyon height Type 2, the temperature contour of canyon road surface received almost

495 60.0 % identical throughout the surface area. During hot summer days, the optimum

496 RPSC embedment within asymmetrical canyon height was found to be the centre location

497 and for the asymmetrical canyon height Type 2, the optimum RPSC embedment was

498 alongside the street canyon.

499 (ii) Lower temperature was obtained by the canyon road surface of the asymmetrical canyon

500 height Type 1, as compared to the other two canyon configurations, dominated by the

501 swirling air within the street canyon due to the obstruction of the second building row

502 (Building B).

- 503 (iii) A significantly lower average surface temperature (20.14-23.08 %) was obtained at the
504 location C-1, A-5 and B-5 when comparing asymmetrical canyon height Type 1 with the
505 other two canyon settings.
- 506 (iv) Significant PTC and STR was obtained by embedding RPSC pipes within the
507 symmetrical canyon height and asymmetrical canyon height Type 2 with the average PTC
508 performance ranging between 30.0-49.0 % and not less than 40.0 % STR.
- 509 (v) The PTC and STR of the RPSC pipes within the asymmetrical canyon height Type 1 was
510 approximately 50.0 % lower in terms of the PTC and 15.0 % lower performance in STR
511 behind the other two canyon settings.

512

513 A significant variation of the temperature contour between the three canyon settings was observed,
514 and therefore the RPSC embedment with the length of the pipes oriented parallel to width of the street
515 canyon should be further evaluated to find an optimum performance value in PTC and STR. Not only
516 this, a significant impact was found by increasing the building height on the surface temperature
517 condition and the performance of RPSC system. Thus, evaluation of the building configuration during
518 hot summer day(s) by comparing several heights seems promising to be carried out in the future.

519

520 **Acknowledgement**

521 This research is supported by Energy 2050 under the Faculty of Engineering, The University of
522 Sheffield, United Kingdom. Special gratitude is also given to Malaysia government agency, Majlis
523 Amanah Rakyat (MARA) for the 4 years' scholarship of Malaysian postgraduate PhD study.

524

525

526

527

528

529

530

531

532

533

534 **References**

- 535 [1] R. A. Memon and D. Y. C. Leung, “On the heating environment in street canyon,” *Environ.*
536 *Fluid Mech.*, vol. 11, no. 5, pp. 465–480, 2011.
- 537 [2] R. Priyadarsini, W. N. Hien, and C. K. Wai David, “Microclimatic modeling of the urban
538 thermal environment of Singapore to mitigate urban heat island,” *Sol. Energy*, vol. 82, no. 8,
539 pp. 727–745, 2008.
- 540 [3] P. a. Mirzaei and F. Haghighat, “A procedure to quantify the impact of mitigation techniques
541 on the urban ventilation,” *Build. Environ.*, vol. 47, no. 1, pp. 410–420, 2012.
- 542 [4] Y. Toparlar, B. Blocken, P. Vos, G. J. F. Van Heijst, W. D. Janssen, T. van Hooff, H.
543 Montazeri, and H. J. P. Timmermans, “CFD simulation and validation of urban microclimate:
544 A case study for Bergpolder Zuid, Rotterdam,” *Build. Environ.*, vol. 83, pp. 79–90, 2015.
- 545 [5] G. Levermore and H. Cheung, “A low-order canyon model to estimate the influence of canyon
546 shape on the maximum urban heat island effect,” *Build. Serv. Eng. Res. Technol.*, vol. 33, no.
547 4, pp. 371–385, 2012.
- 548 [6] B. Blocken, J. Carmeliet, and T. Stathopoulos, “CFD evaluation of wind speed conditions in
549 passages between parallel buildings-effect of wall-function roughness modifications for the
550 atmospheric boundary layer flow,” *J. Wind Eng. Ind. Aerodyn.*, vol. 95, no. 9–11, pp. 941–962,
551 2007.
- 552 [7] S. Bottillo, a. De Lieto Vollaro, G. Galli, and a. Vallati, “Fluid dynamic and heat transfer
553 parameters in an urban canyon,” *Sol. Energy*, vol. 99, pp. 1–10, 2014.
- 554 [8] R. A. Memon, D. Y. C. Leung, and C. H. Liu, “Effects of building aspect ratio and wind speed
555 on air temperatures in urban-like street canyons,” *Build. Environ.*, vol. 45, no. 1, pp. 176–188,
556 2010.
- 557 [9] J. Allegrini, V. Dorer, and J. Carmeliet, “Analysis of convective heat transfer at building
558 facades in street canyons and its influence on the predictions of space cooling demand in
559 buildings,” *J. Wind Eng. Ind. Aerodyn.*, vol. 104–106, pp. 464–473, 2012.
- 560 [10] J. Allegrini, V. Dorer, and J. Carmeliet, “Coupled CFD, radiation and building energy model
561 for studying heat fluxes in an urban environment with generic building configurations,”
562 *Sustain. Cities Soc.*, vol. 19, pp. 385–394, 2015.
- 563 [11] N. Nazarian and J. Kleissl, “CFD simulation of an idealized urban environment: Thermal
564 effects of geometrical characteristics and surface materials,” *Urban Clim.*, vol. 12, pp. 141–

- 565 159, 2015.
- 566 [12] K. Li and Z. Yu, “Comparative and combinative study of urban heat island in Wuhan City
567 with remote sensing and CFD simulation,” *Sensors*, vol. 8, no. 10, pp. 6692–6703, 2008.
- 568 [13] J. Allegrini, V. Dorer, T. Defraeye, and J. Carmeliet, “An adaptive temperature wall function
569 for mixed convective flows at exterior surfaces of buildings in street canyons,” *Build.
570 Environ.*, vol. 49, no. 1, pp. 55–66, 2012.
- 571 [14] J. K. Calautit, B. R. Hughes, and S. S. Shahzad, “CFD and wind tunnel study of the
572 performance of a uni-directional wind catcher with heat transfer devices,” *Renew. Energy*, vol.
573 83, pp. 85–99, 2015.
- 574 [15] J. Allegrini, V. Dorer, and J. Carmeliet, “Influence of the urban microclimate in street canyons
575 on the energy demand for space cooling and heating of buildings,” *Energy Build.*, vol. 55, pp.
576 823–832, Dec. 2012.
- 577 [16] Y. Tamura and P. Van Phuc, “Development of CFD and applications: Monologue by a non-
578 CFD-expert,” *J. Wind Eng. Ind. Aerodyn.*, vol. 144, pp. 3–13, 2015.
- 579 [17] G. Antonioni, S. Burkhart, J. Burman, A. Dejoan, A. Fusco, R. Gaasbeek, T. Gjesdal, A.
580 Jäppinen, K. Riikonen, P. Morra, O. Parmhed, and J. L. Santiago, “Comparison of CFD and
581 operational dispersion models in an urban-like environment,” *Atmos. Environ.*, vol. 47, pp.
582 365–372, 2012.
- 583 [18] T. Defraeye, B. Blocken, and J. Carmeliet, “Convective heat transfer coefficients for exterior
584 building surfaces : Existing correlations and CFD modelling,” *Energy Convers. Manag.*, vol.
585 52, no. 1, pp. 512–522, 2011.
- 586 [19] J. Franke, A. Hellsten, H. Schlünzen, and B. Carissimo, *Best practice guideline for the CFD
587 simulation of flows in the urban environment*, vol. 44, no. May. 2007.
- 588 [20] S.-A. Tan and T.-F. Fwa, “Influence of pavement materials on the thermal environment of
589 outdoor spaces,” *Build. Environ.*, vol. 27, no. 3, pp. 289–295, 1992.
- 590 [21] Y. Qin and J. E. Hiller, “Modeling temperature distribution in rigid pavement slabs: Impact of
591 air temperature,” *Constr. Build. Mater.*, vol. 25, no. 9, pp. 3753–3761, 2011.
- 592 [22] V. Bobes-Jesus, P. Pascual-Muñoz, D. Castro-Fresno, and J. Rodriguez-Hernandez, “Asphalt
593 solar collectors: A literature review,” *Appl. Energy*, vol. 102, pp. 962–970, Feb. 2013.
- 594 [23] S. Hasebe, M. Yamikawa, Y and Meiarashi, “Thermoelectric generators using solar thermal

- 595 energy in heated road pavement,” ... , 2006. *ICT'06. 25th ...*, pp. 697–700, 2006.
- 596 [24] H. Wang, S. Wu, M. Chen, and Y. Zhang, “Numerical simulation on the thermal response of
597 heat-conducting asphalt pavements,” *Phys. Scr*, vol. 14041, pp. 11–14, 2010.
- 598 [25] M. A. AL-SAAD, B. A. JUBRAN, and N. A. ABU-FARIS, “DEVELOPMENT AND
599 TESTING OF CONCRETE SOLAR COLLECTORS,” *Int. J. Sol. Energy*, vol. 16, no. 1, pp.
600 27–40, 1994.
- 601 [26] P. Pascual-Muñoz, D. Castro-Fresno, P. Serrano-Bravo, and a. Alonso-Estébanez, “Thermal
602 and hydraulic analysis of multilayered asphalt pavements as active solar collectors,” *Appl.*
603 *Energy*, vol. 111, pp. 324–332, 2013.
- 604 [27] M. D’Antoni and O. Saro, “Massive Solar-Thermal Collectors: A critical literature review,”
605 *Renew. Sustain. Energy Rev.*, vol. 16, no. 6, pp. 3666–3679, 2012.
- 606 [28] R. Borinaga-treviño, P. Pascual-muñoz, D. Castro-fresno, J. José, and D. Coz-díaz, “Study of
607 different grouting materials used in vertical geothermal closed-loop heat exchangers,” *Appl.*
608 *Therm. Eng.*, vol. 50, no. 1, pp. 159–167, 2013.
- 609 [29] H. Wang and Z. Chen, “Study of critical free-area ratio during the snow-melting process on
610 pavement using low-temperature heating fluids,” *Energy Convers. Manag.*, vol. 50, no. 1, pp.
611 157–165, 2009.
- 612 [30] J. A. Alfaro-ayala, G. Martínez-rodríguez, M. Picón-núñez, A. R. Uribe-ramírez, and A.
613 Gallegos-muñoz, “Numerical study of a low temperature water-in-glass evacuated tube solar
614 collector,” *Energy Convers. Manag.*, vol. 94, pp. 472–481, 2015.
- 615 [31] F. R. Mazarrón, C. J. Porrás-prieto, J. L. García, and R. M. Benavente, “Feasibility of active
616 solar water heating systems with evacuated tube collector at different operational water
617 temperatures,” *Energy Convers. Manag.*, vol. 113, pp. 16–26, 2016.
- 618 [32] W. Tian, Y. Wang, J. Ren, and L. Zhu, “Effect of urban climate on building integrated
619 photovoltaics performance,” *Energy Convers. Manag.*, vol. 48, pp. 1–8, 2007.
- 620 [33] D. S. N. M. Nasir, B. R. Hughes, and J. K. Calautit, “A study of the impact of building
621 geometry on the thermal performance of road pavement solar collectors,” *Energy*, vol. 93, pp.
622 2614–2630, 2015.
- 623 [34] D. S. Nasir, B. R. Hughes, and J. K. Calautit, “A CFD analysis of several design parameters of
624 a road pavement solar collector (RPSC) for urban application,” *Appl. Energy*, vol. 186, pp.
625 436–449, 2017.

- 626 [35] B. Blocken, T. Stathopoulos, and J. Carmeliet, “CFD simulation of the atmospheric boundary
627 layer: wall function problems,” *Atmos. Environ.*, vol. 41, no. 2, pp. 238–252, 2007.
- 628 [36] W. Shaopeng, C. Mingyu, and Z. Jizhe, “Laboratory investigation into thermal response of
629 asphalt pavements as solar collector by application of small-scale slabs,” *Appl. Therm. Eng.*,
630 vol. 31, no. 10, pp. 1582–1587, Jul. 2011.
- 631 [37] R. Anniballe, S. Bonafoni, and M. Pichierri, “Spatial and temporal trends of the surface and air
632 heat island over Milan using MODIS data,” *Remote Sens. Environ.*, vol. 150, pp. 163–171,
633 2014.
- 634 [38] Fluent, “ANSYS Fluent 12.0 user’s guide,” *Ansys Inc*, vol. 15317, no. November, pp. 1–2498,
635 2009.
- 636